Chapter 4

Applications of the electron reconstruction algorithm

This chapter presents the behaviour of `ieElRec` in some channels for which a good electron reconstruction is of prime importance for ATLAS. One should understand that the primary goal of the analyses presented here is the study and benchmarking of `ieElRec` and `iPatRec` for relevant physics events. The results are compared to the corresponding sections of the ATLAS *Physics Performance TDR* [3] when the comparison is possible.

All event samples have been generated using PYTHIA 5.7 & JETSET 7.4 event generators [30]. Final state radiation for decays involving the Z^0 boson (which is known to be inadequate in PYTHIA 5.7) was simulated by the PHOTOS package [31]. The same set-up was used for the production of events as that used for the *Physics TDR*: a single photon emission with the IR cutoff set at 1% of the total Z^0 energy.

The detector simulation was performed using the TDR layout and the corresponding DICE [32] production version (CVS tag 1.0.1). The only change was the introduction of the realistic magnetic field (TDR productions were done with a constant solenoidal field in the ID).

4.1 $\mathbf{B^0 \to J/\Psi \to \mathit{ee}}$

Beauty production in a high energy hadron collision is not yet well understood theoretically as proven by the Tevatron measurements. Calculations to a higher order (NNLO) in α_S need to be carried out as their correction is of the same order as that of the NLO. Reference [3]:Sec:15.8.3 gives an overview of the situation, while a detailed study aimed at assuring a consistent Monte-Carlo production for the LHC conditions can be found in [33]. More technical aspects and details of the event generator settings are presented in [34].

As already mentioned in Sec:1.5.2, the level 1 trigger for the B-physics is selected by a muon with $p_T > 6\,\text{GeV}$. Therefore one of the b hadrons was required to decay into $\mu^{\pm}X$, with $|\eta_\mu| < 2.5$. The charge of this muon will also be used for tagging the particle/anti-particle state of the decaying b quark. The other hadron (B^0 or $\bar{B}^0$) is forced to decay into $K^0 J/\Psi$ and further $J/\Psi \to e^+e^-$. The cuts imposed upon the electron and positron in this study are $p_T > 2\,\text{GeV}$ and $|\eta| < 2.5$. In total 32 700 events have been generated.

4.1.1 Sub-selections and efficiencies

The relatively large data sample allows us to make further sub-selections for a detailed study. Some properties of the $e^{\pm}$'s, irrespective of the particle type, were already presented in the introduction to Sec:3.5. Further, the efficiencies of `ieElRec` and ECAL reconstruction have already been scrutinized. Here this separation will not be redone. One should keep in mind though, that inefficiencies of the electron reconstruction for $p_T < 5\,\mathrm{GeV}$ are dominated by the ECAL cluster reconstruction.

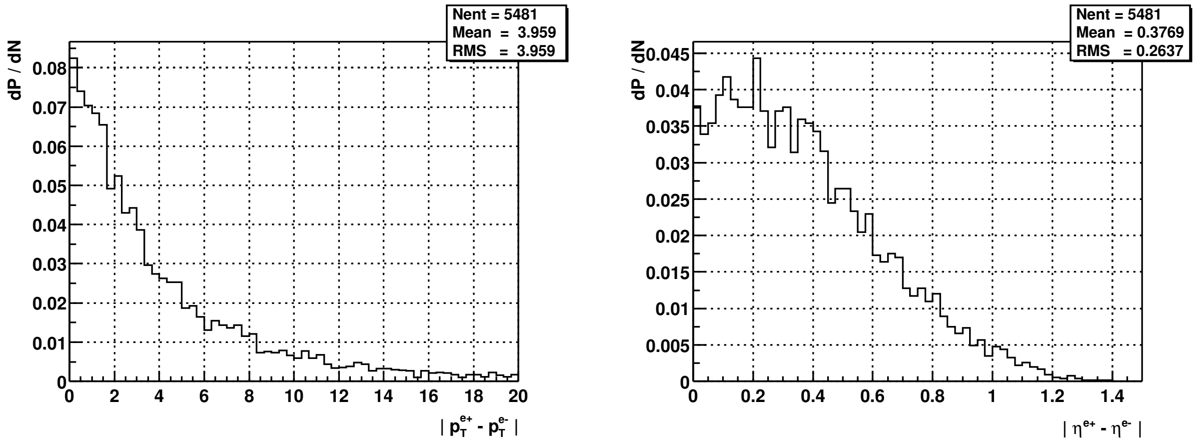

Figure 4.1: Distributions of difference in p_T (left) and η (right) between the $e^{\pm}$ originating from the decay of J/Ψ.

Basically all reconstructed quantities show a strong p_T dependence. While the average p_T of the electron and positron are used for most of the plots, it is still useful to define three sub-selections for results presented in the tables and to unveil the fractions of events belonging to each set of cuts.

Label	Cuts	Fraction
$\mathrm{P_L}$	$p_T < 5\,\mathrm{GeV}$ for both $e^{\pm}$	30%
$\mathrm{P_H}$	$p_T > 5\,\mathrm{GeV}$ for both $e^{\pm}$	25%
$\mathrm{P_I}$	the rest of events	45%

One should combine the left plot of Fig:3.31 (showing a joint distribution of the p_T) with the left plot of Fig:4.1, which shows the distribution of the difference of p_T between electron and positron, to get a firm grip of the situation.

The η dependence due to the geometry of the tracker and its material distribution is also well pronounced. The barrel/transition/end-cap separation is retained, but since now there are two particles covered, five categories have been defined.

Label	Cuts	Fraction
BB	$\lvert\eta\rvert \leq 0.6$ for both $e^{\pm}$	22%
BT	$\lvert\eta\rvert \leq 0.6$ for one of $e^{\pm}$ and larger for the other one	20%
TE	$\lvert\eta\rvert \geq 1.9$ for one of $e^{\pm}$ and smaller for the other one	12%
EE	$\lvert\eta\rvert \geq 1.9$ for both $e^{\pm}$	6%
TT	$0.6 < \lvert\eta\rvert < 1.9$ for both $e^{\pm}$	40%

Again, Figs:3.31 and 4.1 (right plots on both figures) provide a touch of the relevant distributions.

J/Ψ reconstruction efficiency

For each of the aforementioned sub-selections there are further cuts applied to the sum of *pion ambiguities* of both particles ($A_\pi^{ep} = A_\pi^e + A_\pi^p$) and to the invariant mass of the reconstructed J/Ψ ($m_{J/\Psi}$). The behaviour of A_π for single electrons has been studied in Sec:3.4. Values of A_π^{ep} are presented in the range from -2 to 0. The resolution of the $m_{J/\Psi}$ measurement will be discussed in more detail later (Sec:4.1.3); here cuts of ±5, 10 and 20 percent are considered along with the efficiency in the absence of this cut. The results are summarized in Tab:4.1.

$m_{J/\Psi}$ cut	5%			10%			20%			none		
A_π^{ep} cut	-2	-1	0	-2	-1	0	-2	-1	0	-2	-1	0
All	40.22	49.28	53.39	49.60	59.89	64.53	55.64	66.66	71.62	61.44	73.18	78.46
BB	39.48	56.93	66.25	44.55	63.82	74.00	47.32	67.81	78.52	50.02	71.39	82.58
BT	46.21	59.02	64.47	52.72	66.91	72.91	56.01	70.97	77.40	59.70	75.52	82.31
TT	39.88	45.13	46.95	51.15	57.43	59.71	58.49	65.24	67.72	64.92	72.28	74.98
TE	33.75	36.40	37.70	47.98	51.36	52.92	58.20	62.21	63.91	68.30	72.95	74.97
EE	37.26	40.64	41.81	50.28	54.54	55.98	61.07	66.00	67.66	73.31	78.90	80.90
PL	39.23	48.20	52.17	47.68	57.82	62.35	52.63	63.61	68.39	57.53	69.19	74.24
PI	40.67	49.77	54.08	50.01	60.36	65.20	56.53	67.48	72.64	62.18	73.85	79.39
PH	40.57	49.67	53.60	51.08	61.45	65.88	57.52	68.73	73.54	64.61	76.58	81.68

Table 4.1: J/Ψ reconstruction efficiencies for different sub-selections. For each of them different cuts are applied to the A_π^{ep} and reconstructed invariant mass.

4.1.2 Secondary vertex reconstruction

As we are primarily interested in the performance of `ieElRec` no corrections of the track parameters were made (vertex fitting). At this stage it is more important to show what performance can be expected from a *raw* reconstruction as it will serve as an input to any more specialized algorithm.

One should take into account that the resolutions of the perigee parameters improve with the increasing p_T. This is a study at the low-end of the transverse energies that will be used in the ATLAS physics. So it is no surprise that the resolutions of the secondary vertex parameters are rather poor.

To differentiate from the perigee parameters, the quantities describing the secondary vertex are marked by capital letters:

R_0 distance from the origin in the r-φ plane;

Z_0 distance from the origin along the z axis;

P_T, P_L transverse and longitudinal momentum of the decaying particle;

Φ, Θ directional angles of the momentum of the decaying particle.

The search for the secondary vertex was performed in the r-φ plane, by calculating the intersection points of the two circles. The point with a smaller r was selected and the path lengths from the perigee calculated. The Z_0 coordinate was determined by calculating the mean value of the z coordinates predicted by both tracks. This gave better results than using the z coordinate predicted by the track with a higher p_T, although resolutions of z_0 and $\cot\vartheta$ improve with increasing p_T.

P_T and P_L were obtained by transporting the track parameters from the perigee to the intersection point and summing the momenta.

R_0 and Z_0 resolutions

The residual distributions of both quantities have a well pronounced Gaussian center and a rich tail content with about 10% of the events floating outside three standard deviations from the core resolution. Fig:4.2 shows the two residual distributions as a function of the average $|\eta|$ of the $e^{\pm}$ pair. In subsequent discussions the resolutions are obtained by fitting the residual distribution with a Gaussian in the range mean $\pm\, 2 \times$ rms.

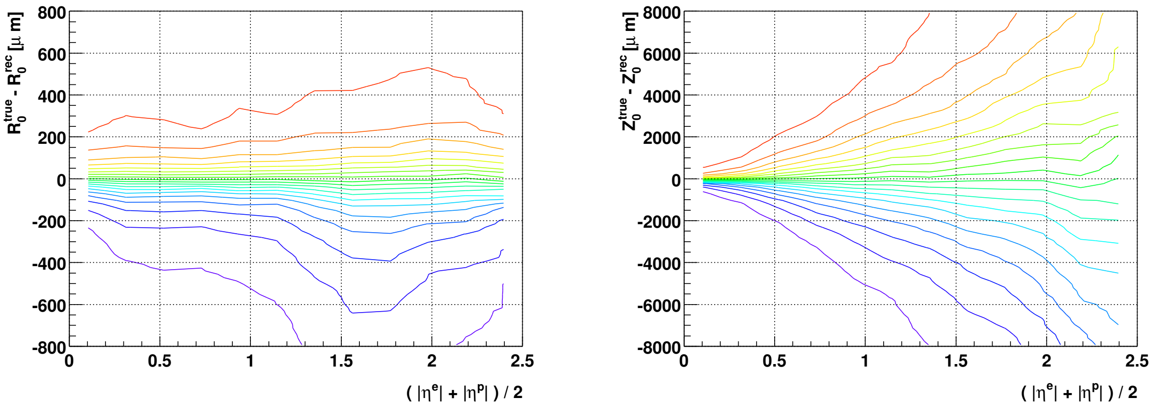

Figure 4.2: Residual distributions of the R_0 (left) and Z_0 (right) measurement. 5% contours are shown (between any two consecutive lines and outside the outer lines, lays 5% of events per x-axis bin).

The distribution of R_0 is exponential with a mean length of 1.75 mm. Resolution of the R_0 measurement as a function of the average $|\eta|$ and p_T is shown in Fig:4.3. It is about a factor of 2 worse than the single track a_0 resolution (taking $p_T = 3\,\mathrm{GeV}$ as a reference value), but one should bear in mind the procedure that leads to the secondary vertex determination and know that the comparison is not exactly fair. The resolution is constant in the barrel region (up to $|\eta| \approx 1$) and then worsens by a factor of approximately 1.5 through the transition region. As a function of the average p_T the resolution deteriorates linearly, degrading by a factor of two in the range from $p_T = 2\,\mathrm{GeV}$ to $10\,\mathrm{GeV}$. Note that the p_T resolution is constant in this energy range and that the a_0 resolution is improving with increasing p_T. Nevertheless, the intersection position is defined poorer and poorer as the tracks get stiffer. Improvement of the order of a few percent can be observed by applying the cuts on the reconstructed invariant mass. Requiring that both particles belong to the **M1b**$^+$ class also improves the resolution. The overall resolution, without applying any cuts, is $\sigma(R_0) = 110\,\mu\mathrm{m}$.

The Z_0 resolution is about ten times worse than the transverse one. Its average value is $\sigma(Z_0) \approx 1.2\,\mathrm{mm}$, which is to be compared to the width of the true Z_0 distribution (Gaussian with $\sigma = 55.6\,\mathrm{mm}$). The dependencies of the resolution on $|\eta|$ and p_T are shown in Fig:4.4. A degradation of the resolution by a factor of ten can be observed over the ID η coverage and by a factor of two over the available p_T range ($2 \nearrow 10\,\mathrm{GeV}$). Basically the same comments

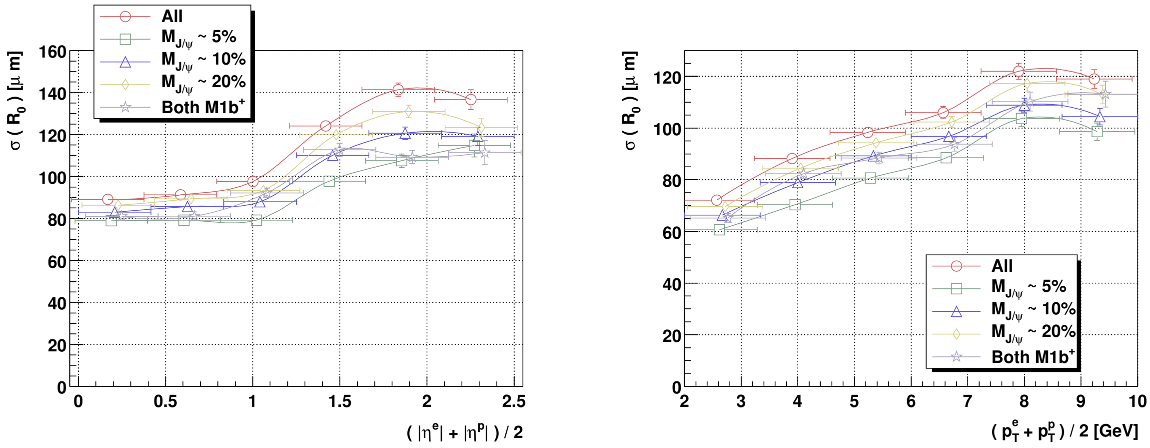

Figure 4.3: $|\eta|$ (left) and p_T (right) dependence of the R_0 resolution. Curves are shown for all events, for three different cuts on reconstructed $m_{J/\Psi}$ ($|\delta m_{J/\Psi}|/m_{J/\Psi}^{\rm true} < 5$, 10, 20%) and for the case when both the electron and positron belong to the **M1b**$^+$ class.

apply as for the R_0 resolution dependence as the intersection position is sought for in the transverse plane. Application of cuts on the reconstructed invariant mass brings only a minor improvement to the resolution.

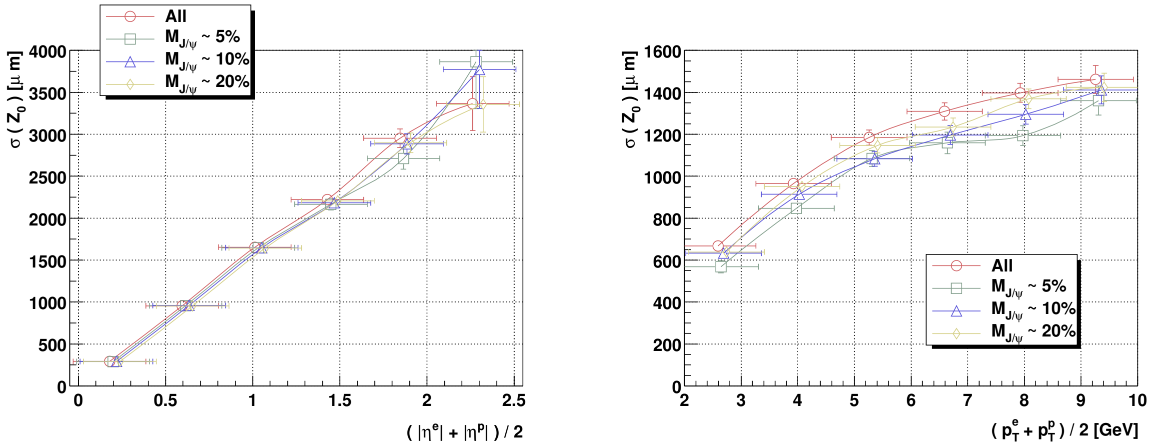

Figure 4.4: $|\eta|$ (left) and p_T (right) dependence of the Z_0 resolution. Curves are shown for all events and for three different cuts on reconstructed $m_{J/\Psi}$ ($|\delta m_{J/\Psi}|/m_{J/\Psi}^{\rm true} < 5$, 10, 20%).

P_T and P_L resolutions

The normalised residual distributions of the P_T and P_L versus the average $|\eta|$ are presented in Fig:4.5. Both quantities exhibit a rather long tail on the 'missing reconstructed momentum' side. There is no dependence on the average transverse energy of the $e^{\pm}$ pair.

The $|\eta|$ dependence of the resolutions of the normalised residuals are shown in Fig:4.6. As expected, the application of cuts on the reconstructed invariant mass improves the resolutions. The 5% cut effectively cancels out the degradation outside the barrel region.

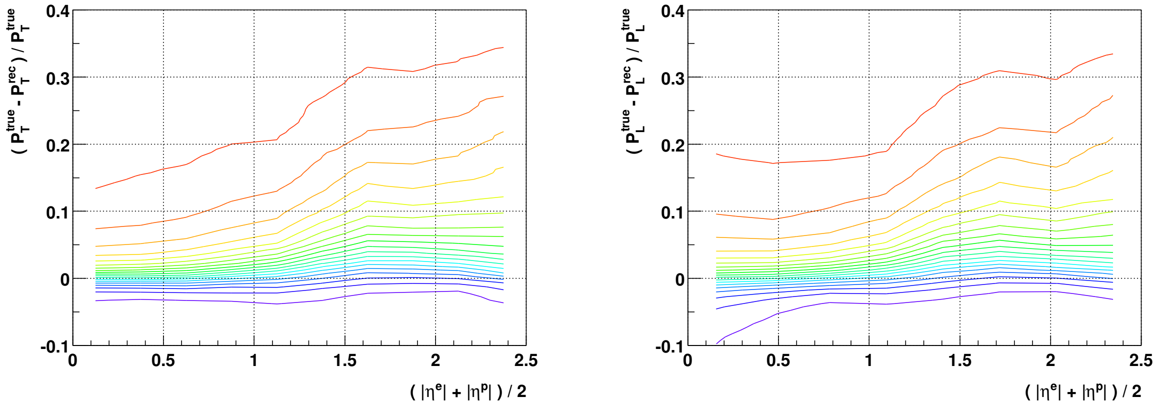

Figure 4.5: Normalised residual distributions of the P_T (left) and P_L (right) measurement as a function of the average $|\eta|$ of the $e^{\pm}$ pair. 5% contours are shown.

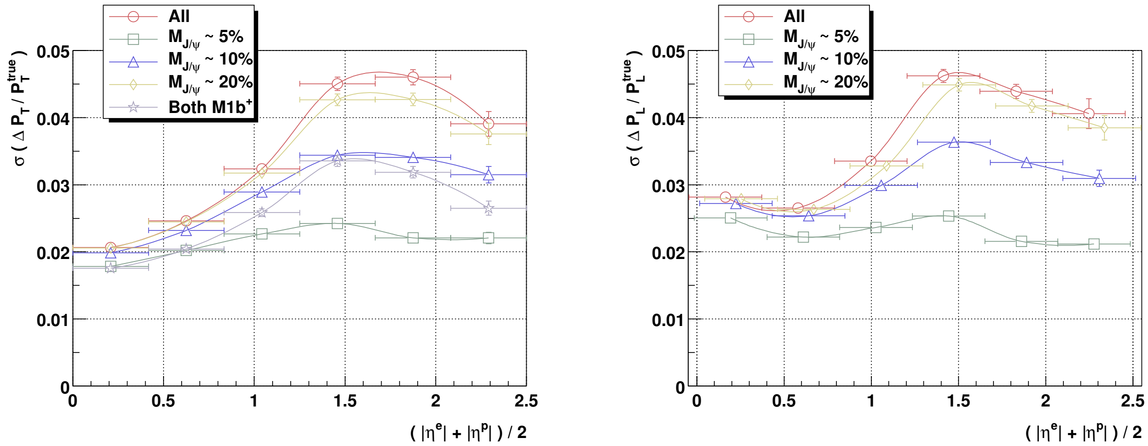

Figure 4.6: Resolutions of the normalised residual distributions of the P_T (left) and P_L (right) as a function of the average $|\eta|$ of the $e^{\pm}$ pair. Curves are shown for all events and for the three different cuts on the reconstructed $m_{\mathrm{J/\Psi}}$ ($|\delta m_{\mathrm{J/\Psi}}|/m_{\mathrm{J/\Psi}}^{\mathrm{true}} < 5$, 10, 20%). For the P_T case the resolution for the sub-sample when both tracks belong to the **M1b**$^+$ class is also shown.

Angular resolution

The resolutions of the measurements of the direction angles in the transverse (Φ) and r–z planes (Θ, expressed as $\cot\Theta$) are shown in Fig:4.7. Compared to the resolutions of single particles (see Sec:3.3.4) the Φ resolution is about five times worse and the $\cot\Theta$ one is degraded by a factor of two. Again, the comparison is not exactly fair, as the angular parameters of the secondary vertex are obtained by transporting the perigee parameters to the reconstructed vertex and in the process we pick up every possible experimental error. The cut on the reconstructed $m_{\mathrm{J/\Psi}}$ improves the resolutions in the transition and end-cap regions.

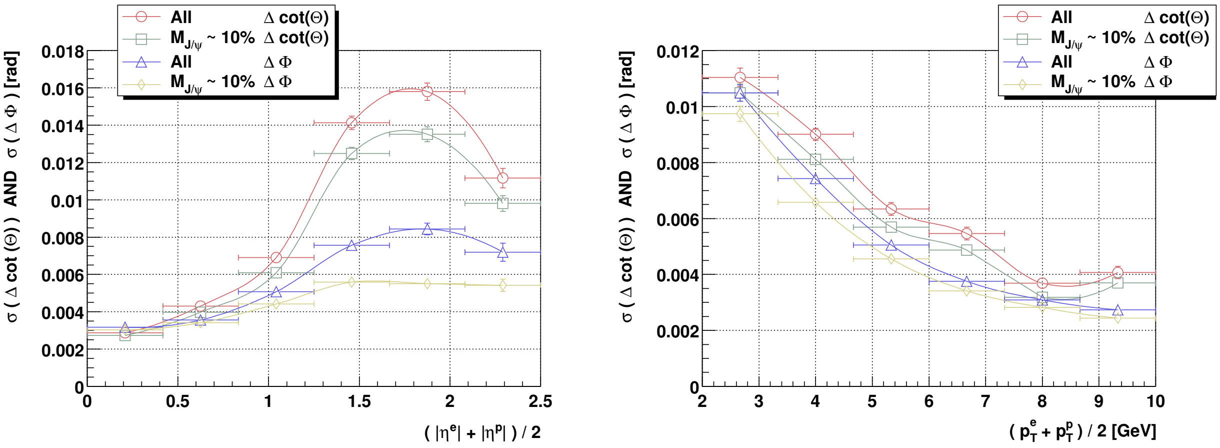

Figure 4.7: Resolutions of Φ (blue and yellow curves) and $\cot\Theta$ (red and green) as a function of the average $|\eta|$ (left) and p_T (right).

4.1.3 $m_{J/\Psi}$ resolution

Finally, we arrive to the gem stone of this analysis, to the reconstruction of the invariant mass of the J/Ψ resonance. To begin with, the distributions of the reconstructed $m_{J/\Psi}$ are presented in Fig:4.8. As the $|\eta|$ dependence is the most pronounced effect, we will further study the position of the peak value and the width of the distribution as a function of pseudo-rapidity.

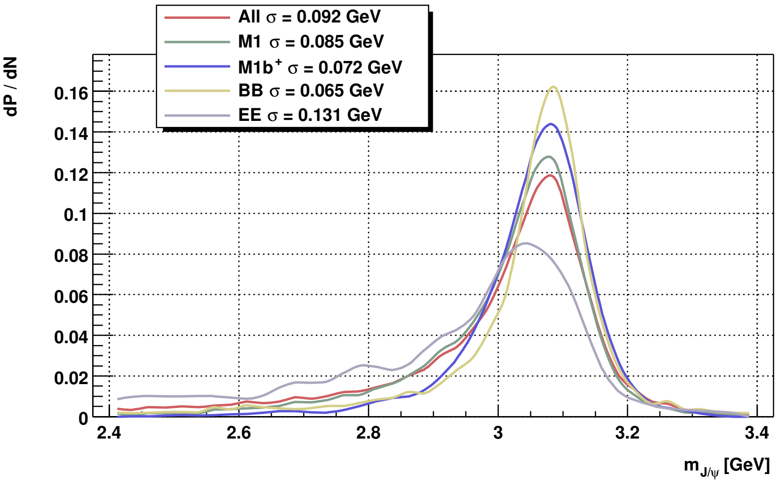

Figure 4.8: The distributions of the reconstructed $m_{J/\Psi}$ for all events and for two different kinds of sub-selections: a) for the cases when both the electron and positron belong to the **M1** or **M1b**$^+$ class; b) for the pure barrel (BB) and pure end-cap (EE) regions. The resolutions obtained by fitting them with a Gaussian in the range mean $\pm 2 \times$ rms are appended to the legend.

But before we plunge into the gaussological description, some attention must be paid to events that populate the tails of the distributions as they will be neglected when their cores are studied. Fig:4.9 presents the raw distributions of the reconstructed $m_{J/\Psi}$. By requiring both particles to belong to the **M1** class, the tail extension is reduced by a factor of two in the barrel region. This factor increases through the transition region and reaches a value of three in the end-cap.

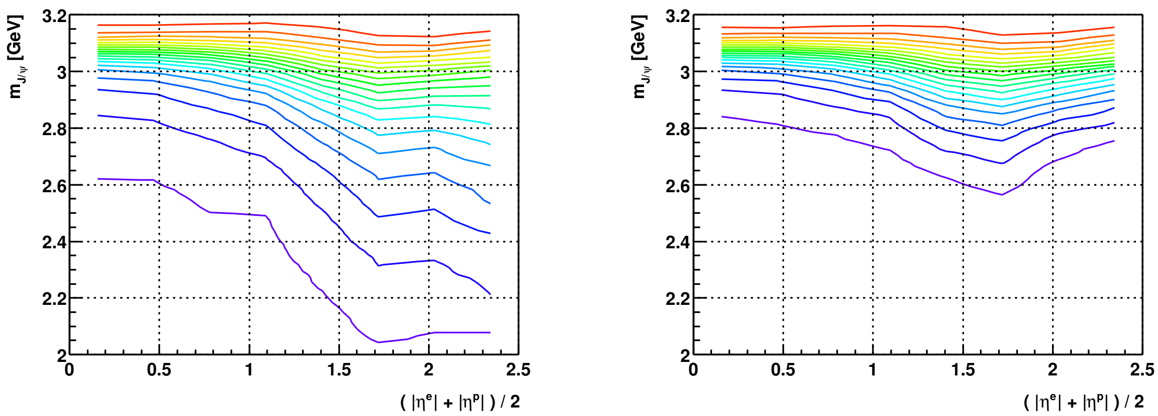

Figure 4.9: 5% contours of the reconstructed $m_{J/\Psi}$ versus the average $|\eta|$. Left: all events, right: both $e^{\pm}$ belong to the **M1** class.

The mean values and resolutions obtained by fitting the cores (mean $\pm 2 \times \mathsf{rms}$) with a Gaussian are shown in Fig:4.10. Both quantities show a direct dependence on the thickness of the tracker. By choosing the **M1** (**M1b**$^{+}$) sample, a substantial improvement in the resolution and mean value can be observed, especially in the end-cap region where the improvement is of the order of 10% (25%).

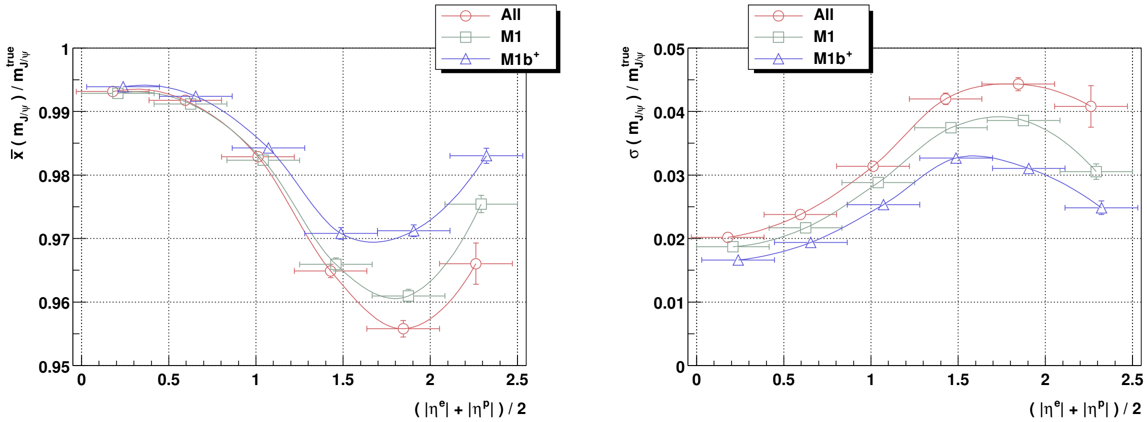

Figure 4.10: The mean values (left) and the resolutions (right) of the Gaussian fit to the reconstructed $m_{J/\Psi}$ as a function of the average $|\eta|$. All events and the sub-samples with both particles belonging to **M1** and **M1b**$^{+}$ are shown.

Here we can compare the obtained $m_{J/\Psi}$ shape to the one presented in the B-physics chapter of the Physics TDR ([3]:Sec:17.2.2). As the resolution quoted in the TDR was obtained by fitting the Gaussian curve over the symmetric core and tail-less side only, it is better to compare FWHMs. `ieElRec` wins with 150 MeV (for all reconstructed events) against 190 MeV presented in the TDR. Tail content is also reduced by a factor of two.

4.2 $\mathbf{Z \rightarrow ee}$

The $Z \rightarrow ee$ events will form the basis of stand-alone ECAL calibration on the electro-weak scale. The results of a calorimeter-only study are presented in [2]:Sec:4.6 and [3]:Sec:12.3.1. There are some concerns expressed about the impact of the *final state radiation* (FSR) and hard ID bremsstrahlung on the uncertainty of the absolute electron energy scale. Here we present a complementary study, arguing how the ID measurements can contribute to the overall performance of the ATLAS detector for this specific process.

A total of 30 000 events have been simulated using the generator and detector simulation settings described in the introduction to this chapter. Furthermore, both the electron and positron were required to have $|\eta| < 2.5$ and $p_T > 5\,\text{GeV}$. As reconstruction of electrons depends crucially on p_T and $|\eta|$, the relevant distributions are presented in Fig:4.11.

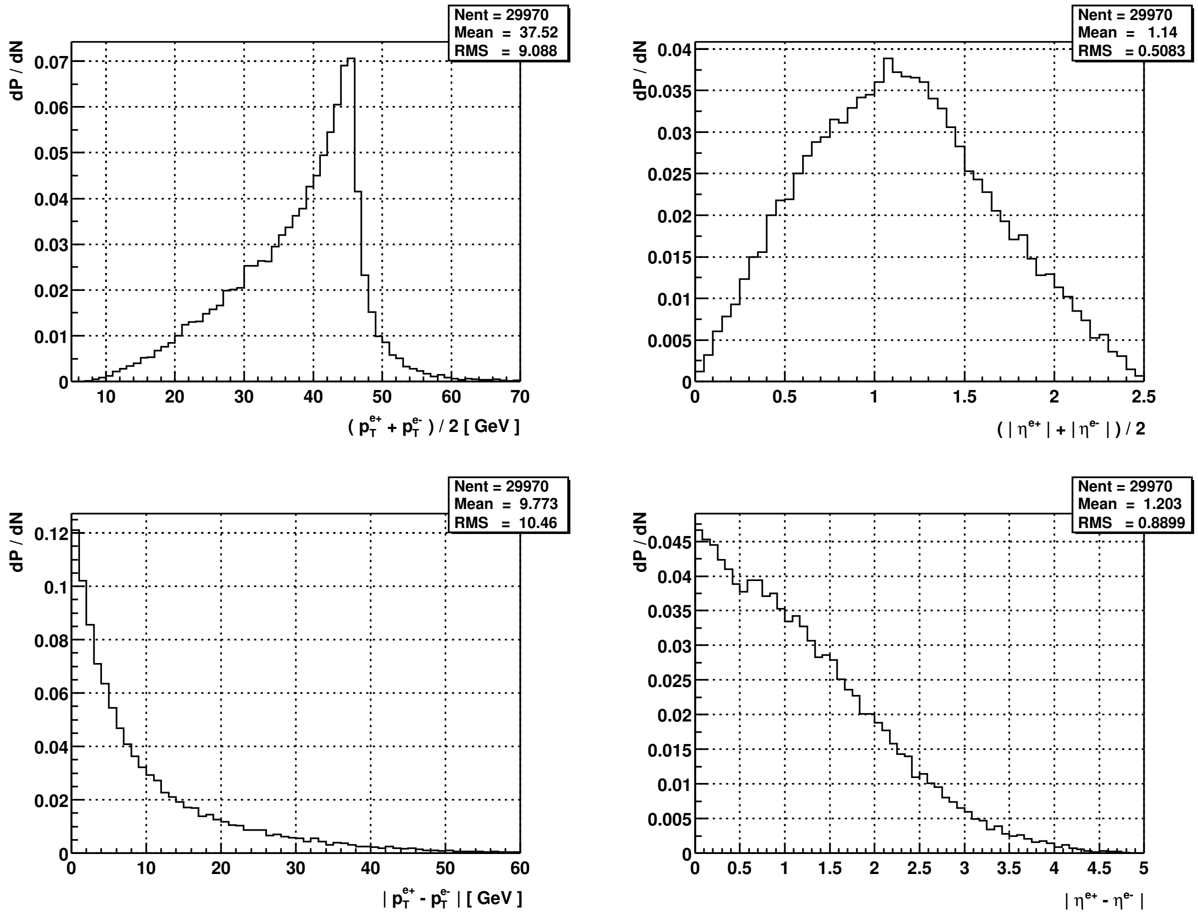

Figure 4.11: Distributions of average values of p_T and $|\eta|$ for the $e^{\pm}$ pair (top). Distributions of absolute values of differences in p_T and η (bottom). All plots show the generated quantities with FSR photons already 'emitted'.

Since the problems connected with FSR and bremsstrahlung are a major issue, the overall effects of both misfortunes will first be compared. Fig:4.12 makes a comparison of the reconstructed m_Z using different sources. The ECAL reconstruction should in principle manage to collect most of the radiated photons. Next, the reconstruction from the KINE banks is already plagued by the missing FSR photons. Both previous cases should be compared to the 'corrected KINE' case (labeled as wFSR) where FSR photons were excavated and their momenta added to the $e^{\pm}$ ones (this should in principle show PYTHIA's idea of the Z^0 shape). Reconstruction in the ID is a victim of both FSR and early bremsstrahlung and is also compromised by a poorer p_T resolution of about 5% (the energy resolution of the ECAL is about 2% in the relevant region).

The reconstruction efficiencies are the next matter of general concern. A division into barrel, transition and end-cap regions (as defined in Sec:4.1.1) is adopted again, with the addition of a new category named **BE** to cover the cases with one e in the barrel and the other one in the end-cap region. As the invariant mass cut will be used to pinpoint the Z^0 events, three invariant mass cuts are studied (5, 10 and 15%). The details of the invariant mass reconstruction are described in later sections. Efficiencies for good ID–ECAL match types are also presented. Tab:4.2 provides the numbers. For readers not too keen on tabular material, the results can be summarized by saying that the efficiency varies from about 50% (with a 5% cut on the reconstructed m_{Z^0} and requiring a good ID–ECAL match for both electrons) to 94.7% (with both electrons reconstructed in the ID but without applying any cuts).

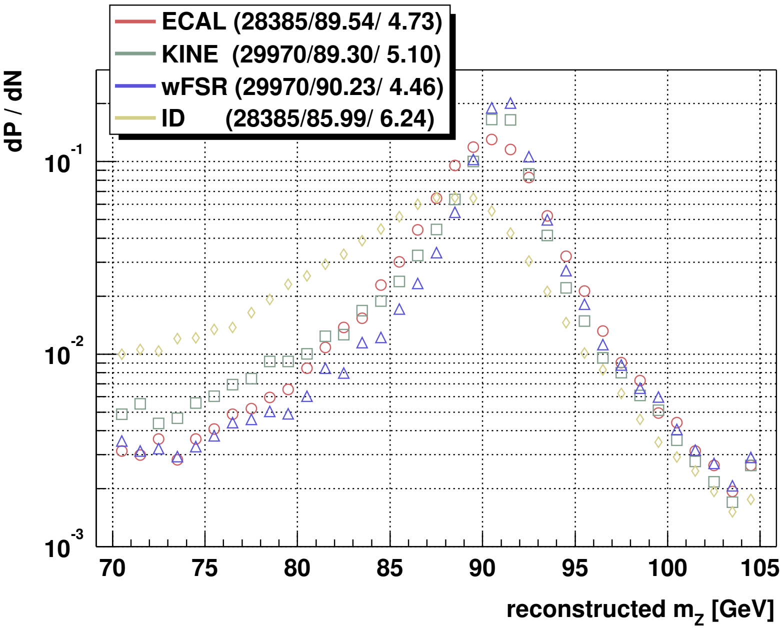

Figure 4.12: Comparison of distributions of the reconstructed m_Z using different available information. The ECAL plot was obtained by using E_T measurement of the calorimeter and direction measurements from the tracker. For the KINE plot information from the generation banks for the $e^{\pm}$ pair was used; for the wFSR plot the FSR photon momenta are included. The ID plot is what `ieElRec` manages to reconstruct without applying any quality cuts. All plots are labeled with their number of entries, mean values and `rms`'s of the distributions.

4.2.1 Reconstruction of vertex parameters

While the EM calorimeter has a better E_T resolution, the tracker outperforms it in measurement of the z vertex position (a factor of 300 in resolution) and directional parameter $\cot\vartheta$ of the tracks in the r-z plane (an improvement in resolution by a factor of about 20). The

m_{Z^0} cut	5%			10%			15%			none		
Match type	All	M1	M1b$^+$	All	M1	M1b$^+$	All	M1	M1b$^+$	All	M1	M1b$^+$
All 100.0	68.87	51.90	38.61	82.81	61.84	45.93	87.32	65.09	48.31	94.71	69.98	51.91
BB 8.0	72.80	55.69	41.67	84.94	64.35	48.08	88.95	67.41	50.29	96.65	72.30	53.77
BT 30.7	70.80	54.80	40.50	84.22	64.61	47.52	88.83	67.99	49.87	96.09	72.79	53.47
TT 28.0	67.97	52.71	39.90	83.14	63.74	48.05	87.54	66.99	50.54	95.23	72.32	54.41
TE 19.5	66.04	47.67	34.97	81.10	58.06	42.98	85.88	61.46	45.66	92.88	66.11	49.13
EE 4.1	66.83	44.55	32.84	77.97	51.68	37.76	81.65	53.97	39.15	89.35	58.39	42.10
BE 9.8	68.63	48.88	36.10	81.10	57.38	42.42	85.86	60.57	44.56	93.20	65.16	48.03

Table 4.2: Z^0 reconstruction efficiencies for different $|\eta|$ sub-selections. For each of them different cuts are applied to the $e^{\pm}$'s match type and reconstructed invariant mass.

radial distance of the Z^0 vertex is much better constrained by the beam width ($20\,\mu$m at low luminosity and $15\,\mu$m at high luminosity operation) and there is not much more one can do.

Again, capital letters are used to denote vertex parameters in order to differentiate them from track parameters.

A precise reconstruction of the Z_0 coordinate of a vertex is important for resolving the ambiguities in the assignment of tracks to different vertices. As Z^0 decays will be the bread and butter of LHC physics, it is important to know the precision which can be expected from ID reconstruction. Fig:4.13 shows the $|\eta|$ dependence of the Z_0 coordinate of the vertex. The overall Z_0 resolution is $\sigma(Z_0) = 75\,\mu$m.

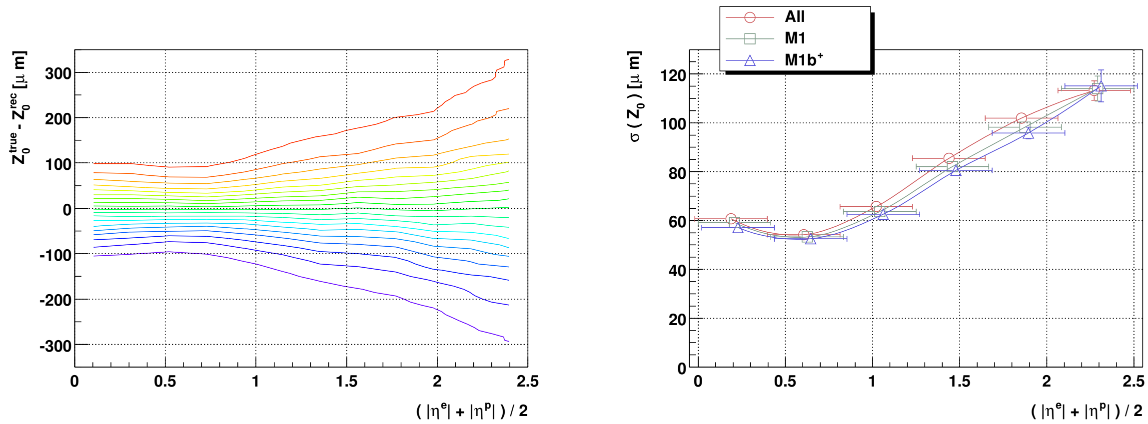

Figure 4.13: The $|\eta|$ dependence of the Z_0 measurement. The residual distribution with 5% contour lines is shown in the left plot and resolutions in the right one.

The main contribution to the error on the reconstructed invariant mass comes from the p_T (or E_T) resolution. Nevertheless, a good reconstruction of the tracks' direction at the vertex is still important. Also, one must know its resolution to correctly account for the experimental error. Although the resolution of the $\cot\vartheta$ measurement has already been studied in Sec:3.3.4, it is presented again for the electron/positron sample provided from Z^0 decays. Fig:4.14 presents its dependence on the average $|\eta|$ of the $e^{\pm}$ pair. The overall resolution is $\sigma(\cot\vartheta) = 0.089 \cdot 10^{-2}$.

The directional parameter φ of the $e^{\pm}$ tracks is measured by the tracker to a higher precision ($\sigma_{\mathrm{ID}}(\varphi) \sim 0.2 \cdot 10^{-3}\,$rad in the relevant p_T region, see Sec:3.3.4) but one must be careful to check if a hard FSR or a hard early bremsstrahlung is lurking behind the curtain.

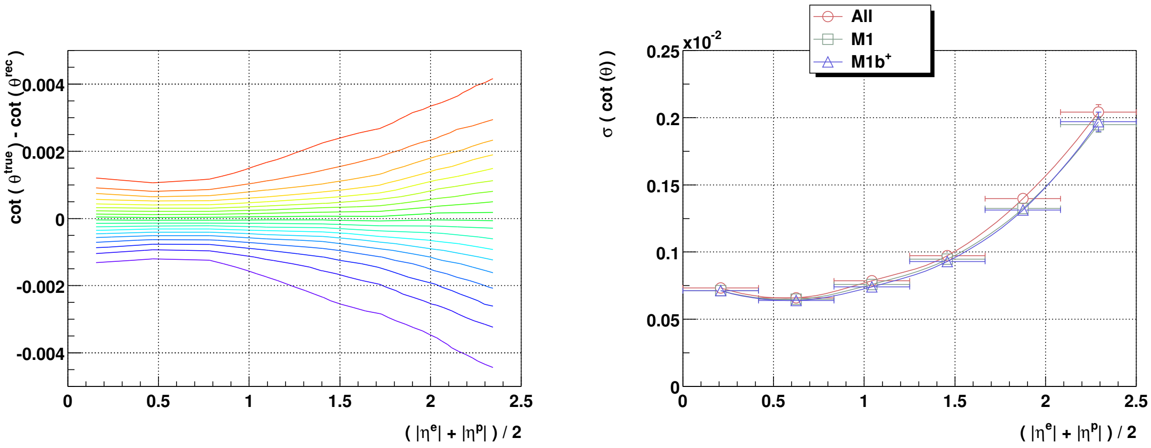

Figure 4.14: The $|\eta|$ dependence of the electron's and positron's $\cot\vartheta$ measurement. Residual distribution is shown in the left and resolutions in the right plot.

A correction based on ECAL φ measurement was attempted for cases when an electron track was not of the **M1b** match type, but the obtained resolution was worse than without applying any correction.

Warning: For the following results the directional parameters of the $e^{\pm}$ tracks used for the vertex reconstruction were always obtained from the ID. The p_T measurement was taken from the ECAL, unless explicitly stated otherwise.

Z^0 momentum reconstruction

A good Z^0 momentum reconstruction is of prime importance for the reconstruction of the invariant mass of particles decaying to Z^0. The $H \to ZZ^{(\star)} \to 4e$ decay, presented in the next section, is one of its most prominent clients.

The residual distributions of the directional angles $\cot\Theta$ and Φ as well as dependence of their resolution on average $|\eta|$ of the $e^{\pm}$ pair are presented in Fig:4.15. Both distributions are exhibiting tails that would make any peacock die of envy. The central resolution (obtained by fitting the residual distribution with a Gaussian curve in the range $\pm\ 2 \times$ rms) of the $\cot\Theta$ measurement is $\sigma(\cot\Theta) = 0.218$ and $\sigma(\Phi) = 0.052\,\text{rad}$ for the Φ measurement. The resolution of $\cot\Theta$ shows a strong dependence on average $|\eta|$. A seemingly unnatural goodness of the resolution at low $|\eta|$ can be explained by the fact that only the Z^0's produced with a low longitudinal momentum in the detector's reference frame can decay so that both the electron and positron have low $|\eta|$.

Distributions of transverse (P_T) and longitudinal (P_L) momentum of generated Z^0's are both approximately exponential with mean values of $\tau(P_T) \sim 16\,\text{GeV}$ and $\tau(P_L) \sim 137\,\text{GeV}$. Normalized residual distributions of both quantities are shown in Fig:4.16. As expected, the ECAL measurement (using directional parameters as reconstructed by the tracker) is more precise and almost unbiased by the early photon emission. On the other hand, the ID stand-alone reconstruction is plagued by a systematic shift and an asymmetric tail toward the missing momentum side. Sub-selections with good match classes give better results, but can't really do much to remedy the situation. For the case when p_T is taken from the ECAL these sub-selections provide only a minor improvement. The resolution of the P_T

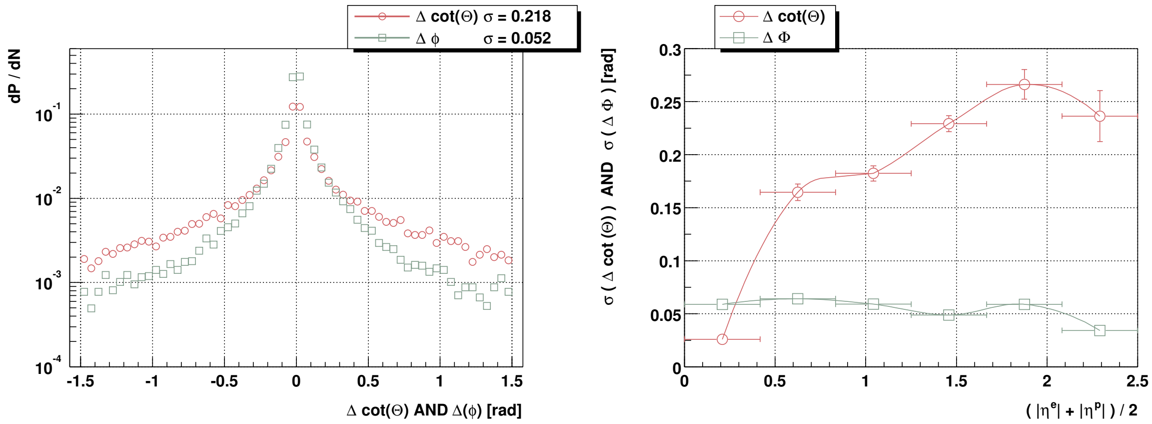

Figure 4.15: The angular parameters of the Z^0's momentum. Overall residuals of the $\cot\Theta$ and Φ measurements are presented in the left plot. The right plot show the dependence of their resolutions on the average $|\eta|$ of the $e^{\pm}$ pair.

measurement using ECAL's p_T measurement is $\sigma(P_T) = 5.2\%$ and $\sigma(P_L) = 2.5\%$ for the P_L measurement.

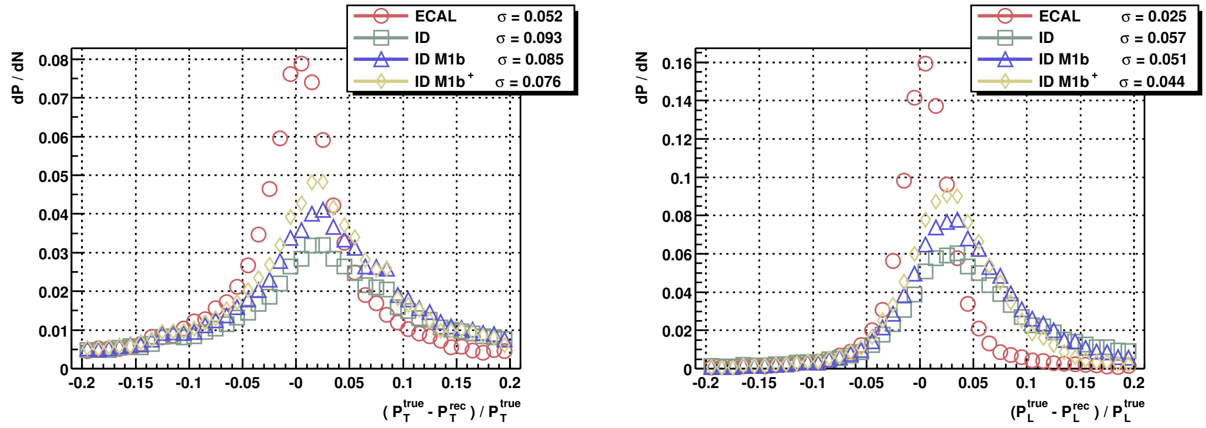

Figure 4.16: The normalized residual distributions of transverse (P_T, left) and longitudinal (P_L, right) momentum of the Z^0 vertex. Labels ECAL and ID denote the origin of the p_T measurement only. For the ID all events and cases when both $e^{\pm}$ belong to match type **M1b** and **M1b**$^+$ are shown.

4.2.2 m_{Z^0} resolution

As the width of the Z^0 resonance is comparable to the expected resolution of the m_{Z^0} measurement, it is more instructive to study the resolution of the reconstructed m_{Z^0} with respect to the generated $m_{Z^0}^{\text{gen}}$. Distributions of the generated and reconstructed m_{Z^0} were already presented in the introduction (see Fig:4.12).

It has been shown in the previous sections that due to FSR we can't hope for a good m_{Z^0} measurement relying on the ID alone. The adopted procedure has been explained in the previous section (see the warning). The left plot of Fig:4.17 shows the distribution of the reconstructed m_{Z^0} as a function of the average $|\eta|$ of the $e^{\pm}$ pair. There is no dependence on $|\eta|$ and the tails are well behaved over all the ID coverage. The right plot shows the normalized residual distribution of the same quantity, produced by using the generated $m_{Z^0}^{gen}$ on a per event basis. It serves to estimate the expected tail content. Mean values and resolutions, obtained by fitting $|\eta|$ slices with a Gaussian in the range mean $\pm 2 \times \mathsf{rms}$, are presented in Fig:4.18. While the behaviour of the mean value is a question of calibration in the used version of ECAL reconstruction code, the dependence of the resolution gives a measure of the effective broadening of the reconstructed Z^0 shape ($\Gamma_{Z^0} = 2.49\,\mathrm{GeV}$). In the barrel section the natural width and the experimental resolution are approximately the same, while in the transition region of the ID the experimental resolution is worse by 60%.

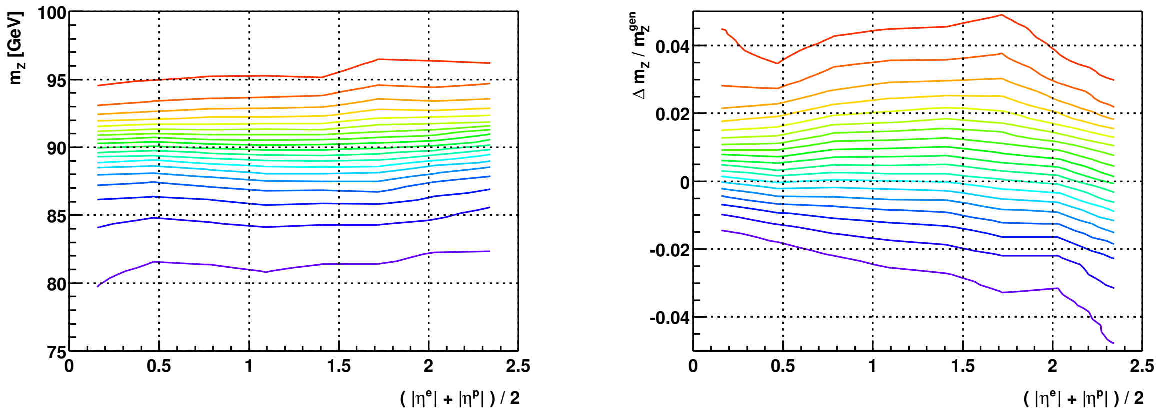

Figure 4.17: Left: 5% contour lines of the reconstructed m_{Z^0}. Right: 5% contour lines of the normalized residual distribution of the reconstructed m_{Z^0} with respect to the generated m_{Z^0}. Both quantities are plotted versus the average $|\eta|$ of the $e^{\pm}$ pair.

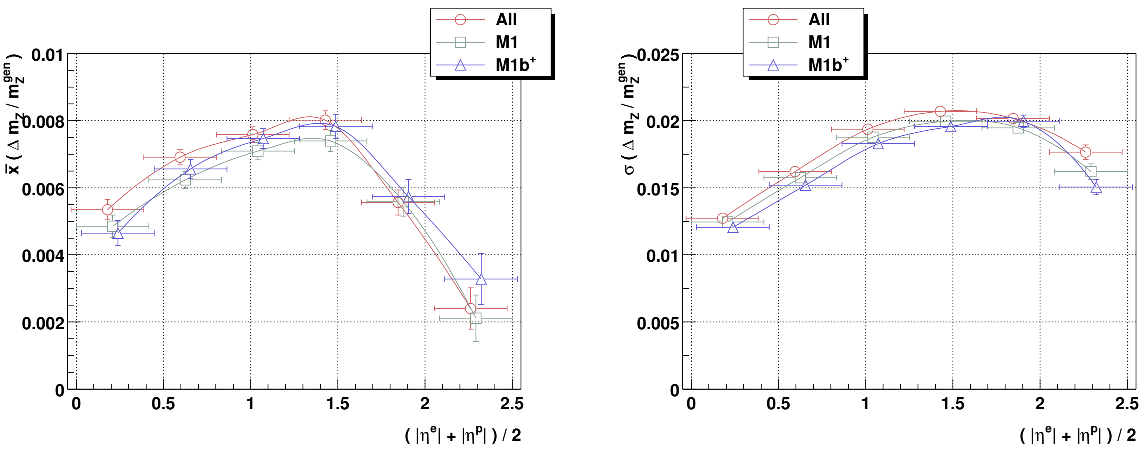

Figure 4.18: Mean values (left) and resolutions (right) of the normalized residual distribution of reconstructed m_{Z^0} versus the average $|\eta|$ of the $e^{\pm}$ pair. Curves are shown for all events passing the `ieElRec` reconstruction and for those with both electron and positron belonging to the **M1b** and **M1b**$^{+}$ class.

To compare the results to those presented in the TDR section “Calorimeter performance and calibration with $Z^0 \to ee$ events” ([2]:Sec:4.6) additional event selections must be done.

Firstly, events containing a hard FSR photon were omitted from their analysis. Since this separation can only be done using the information from the generation banks, some shadows of doubt are cast on the realism of the TDR results. And secondly, the events containing electrons in the ECAL's crack region ($1.37 < |\eta| < 1.52$) were not considered. Following the same steps the obtained resolution is $11.7\%/\sqrt{E}$ (see Fig:4.19) while the one quoted in the TDR is $11.4\%/\sqrt{E}$. However, the tail content outside the Gaussian tail is reduced by a factor of 3.

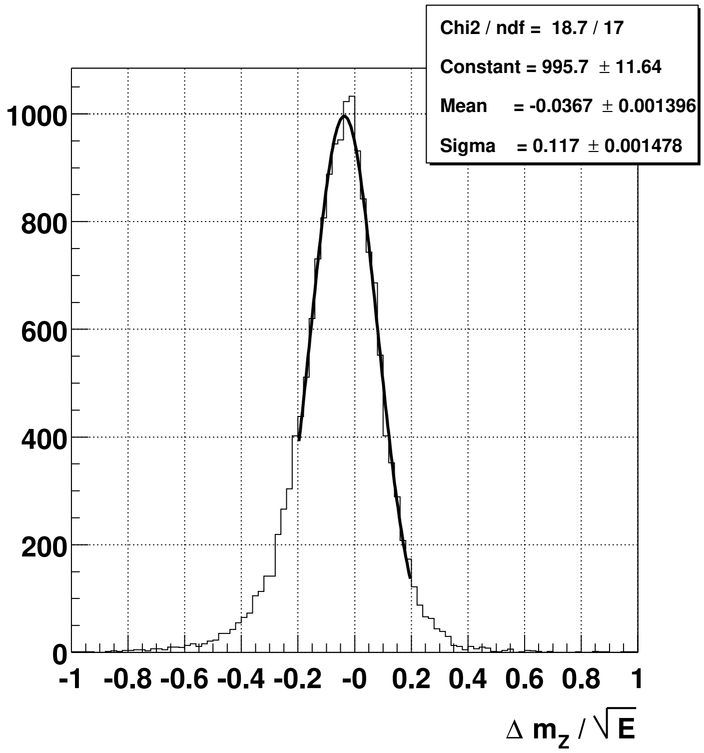

Figure 4.19: Difference between the reconstructed energy in the calorimeter and the true energy, divided by the square root of the true energy, as obtained for electrons from Z^0 decays.

4.3 H $\rightarrow$ ZZ$^{(\star)}$ $\rightarrow$ 4e

As a discovery of the Higgs boson in any form (even its absence) is one of the primary goals of the LHC project, it seems rather unnecessary to make much further introduction. The following study of the SM Higgs decay to four electrons complements the results presented in the *Physics TDR* by putting more emphasis on the ID reconstruction ([3]:Sec:19.2.5 (H $\rightarrow$ ZZ* $\rightarrow$ 4l) and [3]:Sec:19.2.9 (H $\rightarrow$ ZZ $\rightarrow$ 4l)). Detailed electron p_T distributions are presented and the role of the ID in their reconstruction is discussed together with its impact on the reconstruction of the Higgs boson mass.

10 000 events for each of $m_{\rm H}$=(130, 150, 180, 200 GeV) were simulated using the generator and detector simulation settings described in the introduction to this chapter. Associated W and Z productions were not included in the event generation (their cross-section is about 50 times smaller). The production is dominated by gluon fusion ($\sim$ 70%) and WW fusion ($\sim$ 20%). The H boson was forced to decay into Z$^{(\star)}$Z$^{(\star)}$. Both Z's were allowed to be off-shell, mainly out of curiosity, since this effect is below 1% even with the lowest value of $m_{\rm H}$ (also, standard ATLAS analysis cuts require one Z to be close to m_{Z^0}). Furthermore, rather obviously, both Z's were forced to decay into two electrons. All electrons were required to have $p_T > 5$ GeV (before FSR corrections were applied) and $|\eta| < 2.5$.

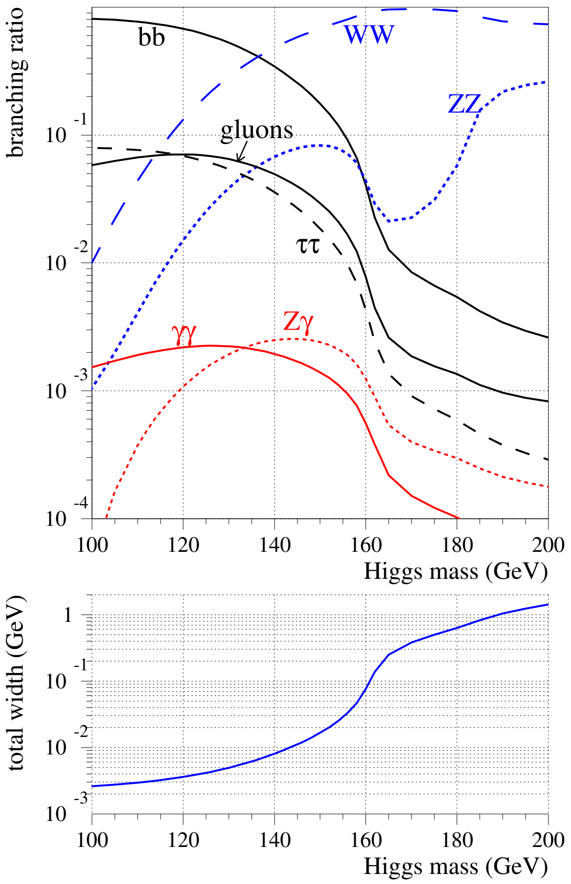

Figure 4.20: Branching ratios and full width of the SM Higgs boson as obtained from the HDECAY package.

The full width and branching ratios of the SM Higgs boson vary rapidly through the studied region. Their behaviour, as obtained by the HDECAY package ([35]), is shown in Fig:4.20. When considering branching ratios remember that the LHC environment is 'full of jets' and that the $b\bar{b}$ decay channel is only considered with an associated W or Z production and a leptonic decay of the accompanying gauge boson. Decays into gg and $\tau\bar{\tau}$ are not considered at all by ATLAS. For $m_H \sim 200$ GeV the natural width and experimental resolution are getting comparable and it becomes possible to measure Γ_H provided our knowledge of the detector's resolution is sufficient. This measurement provides a direct test for physics beyond the SM as the SM predictions of Γ_H as a function of m_H are firm and unambiguous.

4.3.1 Some peculiarities

This section is a brief survey of some kinematic properties of the system under study. It is meant as a reference for those who will delve in the lower parts of the analysis and will, on occasion, have to think in the context of these distributions.

Kinematics of H

H production mechanisms at the LHC are far from trivial and they result in Higgs bosons produced at different angles toward the beam axis and with a wide range of boosts. Fig:4.21 presents $|\eta|$ distributions and the correlation between this angle and the relativistic γ factor. In general, due to the proton's structure functions, it's hard (or at least very rare) to squeeze more than 1 TeV of energy out of two protons colliding at 14 TeV cms energy. When the Higgs boson is produced at low $|\eta| \lesssim 1.5$, its momentum is generally small. Higher boosts are available at higher $|\eta|$. One should keep in mind though, that this distribution is sliced heavily by the requirement of all electrons having $|\eta| < 2.5$.

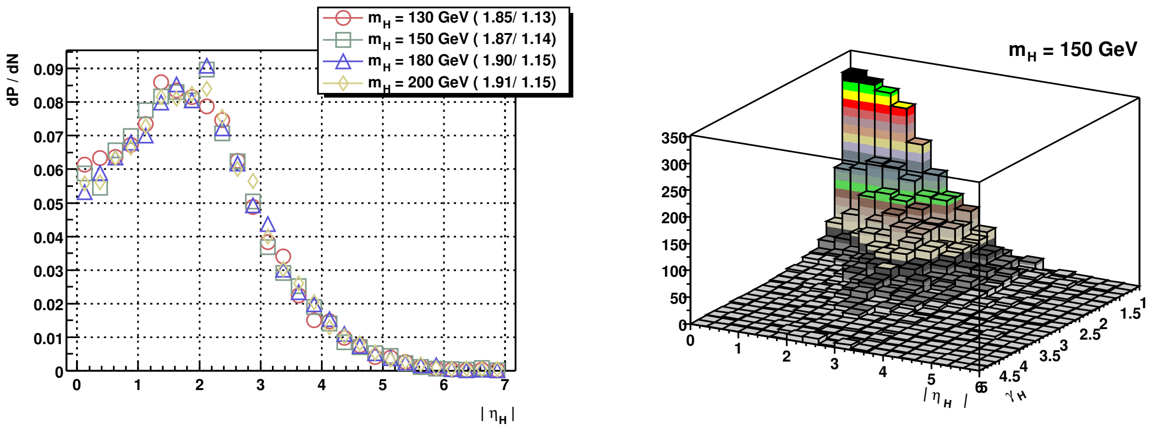

Figure 4.21: Left: $|\eta|$ distributions of the momentum of the generated Higgs bosons. Mean values and rms's are appended on the label. Right: correlation of boost with $|\eta|$ for $m_{\rm H} =$ 150 GeV.

Role of Z*'s

The electron spectrum from singly produced Z's (presented in Fig:4.11) is rather different than the one emanating from H decays. The difference is even more striking in the case of Z* and it implies that a different electron reconstruction approach might be more fruitful for a low mass H.

The first messenger of the fact, that some low-p_T electrons ($p_T < 20$ GeV, where the ID is more precise than the ECAL) show up in the final state can be seen in the invariant mass distribution of the off-shell Z* (Fig:4.22). There are basically no surprises, one should perhaps note that there is a substantial fraction of Z*'s produced at the lower end of the available phase space.

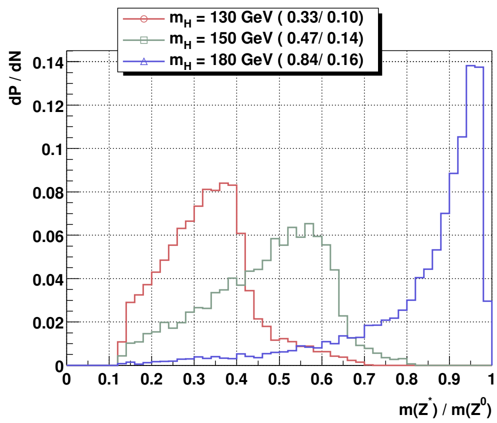

Figure 4.22: Off-shellness of the Z*'s originating from H decays for different m_H.

Fig:4.23 presents the electron p_T and $|\eta|$ distributions from the decays of the lighter of the two Z's. The curve for $m_{\rm H} = 200$ GeV can safely be taken as a representative of the

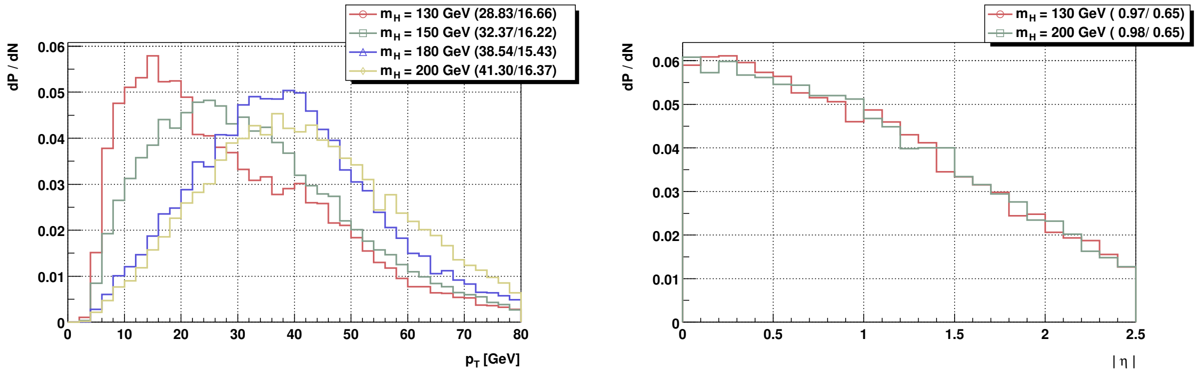

Figure 4.23: p_T (left) and $|\eta|$ (right) distributions of electrons from the Z* decays.

decaying on-shell Z. As far as the p_T distributions are concerned, the most important aspect is the percentage of electrons with $p_T < 20\,\mathrm{GeV}$:

m_H	[GeV]	130	150	180	200
$p_T < 20\,\mathrm{GeV}$	[%]	39	27	13	10

This corresponds to fractional usefulness of the tracker for a p_T measurement used for H reconstruction. One should in principle be careful to check for a hard FSR. In the following analysis the p_T measurement of an electron was taken from the tracker if p_T measured by the ECAL was below 20 GeV and its ECAL/ID match was of the **M1** type with $p_T^{\mathrm{ID}} > p_T^{\mathrm{ECAL}}$. The improvement obtained for the reconstructed $m_{Z^\star}$ is shown in Fig:4.24. The correction is at 1% level and is getting smaller with increasing average $m_{Z^\star}$. Fraction of events, to which the correction is applied, is also falling from about 33% for the Z* sample from $m_{\mathrm{H}} = 130\,\mathrm{GeV}$ to about 9% of cases for on-shell Z's. $|\eta|$ distributions are not influenced by m_{H} or off-shellness of the Z boson.

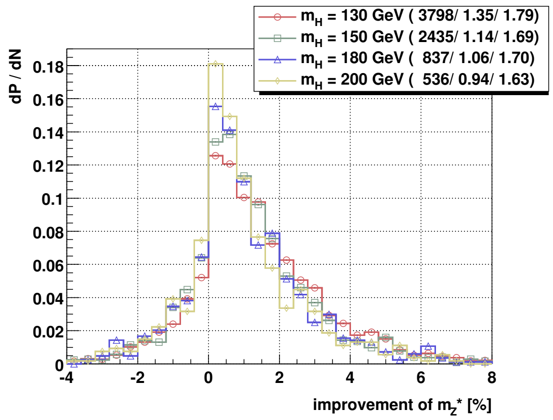

Figure 4.24: Relative improvement (positive values) of the reconstructed $m_{Z^\star}$ by use of tracker's p_T measurement. Distributions are labeled by number of entries, their mean values and rms's.

4.3.2 Reconstruction efficiency

As it is slightly omisive to study efficiency of reconstruction of a yet undiscovered physical system without an accompanying study of background processes, an overview of the situation is provided in the following. The first event pre-selection is done by application of simple kinematical cuts on the p_T of electrons (some already by the trigger) and mass of reconstructed Z$^{(\star)}$'s. For the decay channel under study the reducible background comes from $t\bar{t}$ and Z$b\bar{b}$ productions. Details are studied in [36] and reviewed also in the 'Physics TDR' ([3]:Sec:19.2.5.3). Further rejection of this background is based on calorimeter isolation and cuts on the impact parameter of reconstructed electrons. For the irreducible background, the continuum ZZ* production, some additional separation can be obtained by using the sum of four-lepton transverse momenta and the opening angle between the Z–Z* pair[37].

More technically, as it is hard to apply cuts on non-existent electrons, the use of `ieElRec` provides a 4% improvement of electron reconstruction efficiency which results in a $\sim 10\%$ increase of raw reconstruction efficiency of the H boson. Mainly this increase can be attributed to a better understanding of the electron behaviour in the detector and re-inclusion of some well reconstructed electrons that would fail a more stringent set of requirements. Nevertheless, one should still be concerned about the quality of reconstructed electrons. For an event to be considered efficient, it was required that all electrons belong to **M1** or **M3** ECAL/ID match type. By inclusion of the **M3** match type (ECAL provides a better measurement) it is in part accounted for cases of a hard FSR and early bremsstrahlung. This, of course, must have some impact on the derived reconstructed quantities. To observe this effect, windows of different size were set upon mass of the reconstructed H. Obtained reconstruction efficiencies are dumped in Tab:4.3. For the reconstruction efficiency improvement of 10% quoted above, a 10% cut on m_H was used. As will be seen later, inclusion of the events with **M3** electrons worsens the $m_{\rm H}$ resolution by about 3%. Nothing is for free ...

$m_{\rm H}$ cut	2%			5%			10%			none		
Match type	All	M1/3	M1	All	M1/3	M1	All	M1/3	M1	All	M1/3	M1
m : 130 GeV	60.15	57.71	36.26	83.28	78.47	47.89	87.32	81.32	49.39	89.11	82.11	49.86
m : 150 GeV	62.23	59.61	37.16	83.89	79.29	47.79	87.43	81.91	49.14	89.23	82.87	49.63
m : 180 GeV	61.35	58.74	34.58	81.27	77.25	44.51	85.49	80.88	46.49	88.90	83.09	47.74
m : 200 GeV	63.47	60.51	35.53	82.39	77.87	45.08	86.64	81.45	47.15	89.64	83.49	48.30

Table 4.3: H reconstruction efficiencies for different values of generated $m_{\rm H}$. For each of them different cuts are applied to the $e^\pm$'s match type and reconstructed invariant mass.

In further analysis the same kinematic cuts were applied as enumerated in the 'Physics TDR' ([3]:Sec:19.2.5.1). All electrons were required to have $p_T > 7\,\text{GeV}$ and at least two must have had $p_T > 20\,\text{GeV}$ (level 1 trigger). One of the $e^\pm$ pairs was further required to have its invariant mass within an energy dependent window around $m_{\rm Z^0}$ (from 15 down to 6 GeV) and the invariant mass of the second pair had to be above a certain threshold (from 20 to 60 GeV).

4.3.3 Vertex parameters

Cuts imposed upon impact parameters of all electrons in the final state can serve for rejection of the reducible backgrounds. Since the $pp \to {\rm Z}^0 b\bar{b}$ process was included in Pythia 5.7 as a preliminary feature that was not intended for use in physical analyses, the results presented in the TDR can well happen to be widely off the track with respect to its cross-section and final state kinematics. This particular study will therefore have to be redone with an improved Monte-Carlo generator. Here the results obtained with `ieElRec` are presented with emphasis on their application to the background rejection.

Both longitudinal (z_0) and transverse (a_0) impact parameters of individual e's can be used for secondary b-vertex detection. Displaced b-vertices will occur for ${\rm Z}^0 b\bar{b}$ and $t\bar{t} \to b\bar{b}{\rm W}^+{\rm W}^-$ processes, as both b-quarks must decay into electrons to actually provide the $4e$ signature. Fig:4.25 shows the relevant distributions for $m_{\rm H} = 150\,\text{GeV}$. Statistical values obtained for other event samples deviate from the one presented below 1% level. For the a_0 measurement, the minimum, average and maximal values of its absolute value are shown. While cuts can be applied directly upon the a_0 measurements by using the beam constraint, the Z_0 coordinate of the vertex has first to be determined by using the four independent measurements. The right plot of the figure is a collage of the z vertex coordinate related distributions:

$\boldsymbol{\delta Z_0}$ is a residual distribution of the Z_0 measurement obtained by averaging individual z_0 measurements (a resolution of 50 μm is consistent with the results for single particles);

$\mathbf{Z_A - Z_B}$ is a distribution of difference between the reconstructed Z_0 coordinates of the two Z^0's;

$\mathbf{max(\Delta Z_0)}$ is a distribution of distance between the two most separated electrons.

For the actual rejection one would of course try to use both variables, possibly simultaneously. The exact form of the cuts can only be determined by inspection of the other (back-ground) side of the coin.

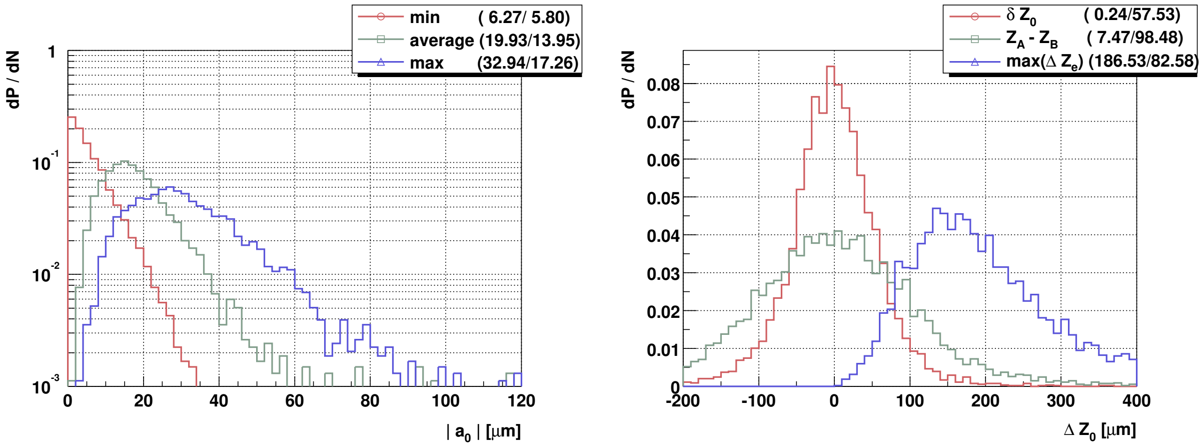

Figure 4.25: Various distributions portraying the reconstruction of single-electron perigee parameters a_0 (left) and z_0 (right) for $\mathrm{H} \to \mathrm{ZZ}^\star \to 4e$ at $m_H = 150\,\mathrm{GeV}$. All plots are labeled by mean values and rms's. Detailed description is interwoven with the text.

4.3.4 α_Z: the Z^0–$\mathrm{Z}^{0(\star)}$ opening angle

As already mentioned, the angle between the reconstructed Z^0 bosons can be used for rejection against the $\mathrm{ZZ}^\star$ background. In the studied range of H's masses there is a chronic shortage of invariant mass and the momentum 'given' to the H's decay products is on average substantially smaller than the original boost of the H boson. This results in a small opening angle α_Z between the two Z^0 bosons as shown in the left plot of Fig:4.26. The residuals of this measurement are presented in the partner-figure. Their distributions are more exponential than Gaussian with a characteristic angular difference of 0.01 rad.

4.3.5 Reconstruction of m_H

The improvement of the $m_{\mathrm{Z}^\star}$ measurement by usage of the tracker's p_T measurement has already been presented and now it's time to assess its impact on the m_H resolution. Another improvement is expected from application of the m_{Z^0} constraint as the experimental invariant mass resolution at the Z^0 resonance is smaller than its width. This constraint is, following the TDR, applied if the mass of the electron pair is within a $\pm 6\,\mathrm{GeV}$ window around m_{Z^0}. Both

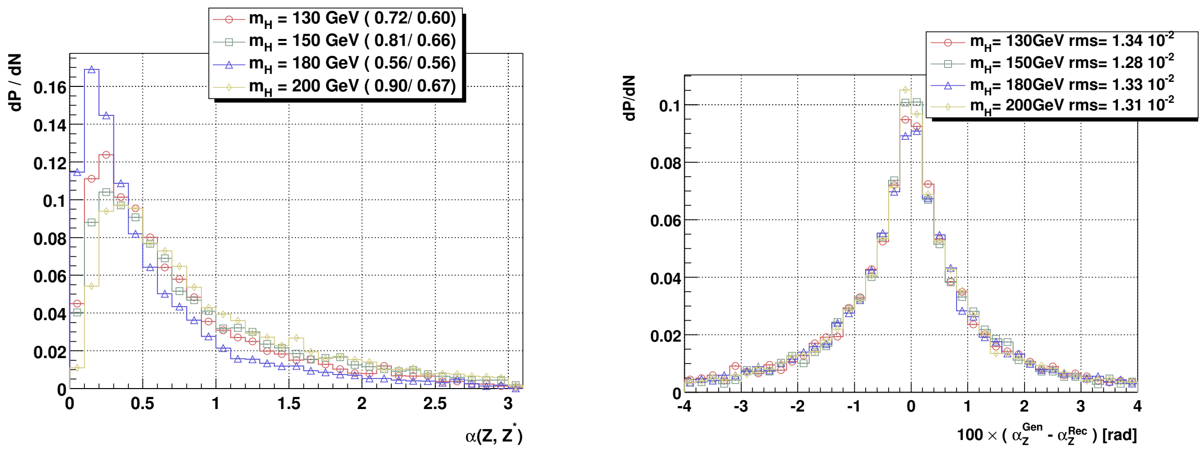

Figure 4.26: Left: distributions of the α_{Z} angle. Right: corresponding residual distributions labeled by their rms's.

corrections are compared in Fig:4.27, which shows raw m_{H} distributions for $m_{\mathrm{H}} = 130\,\mathrm{GeV}$ and $180\,\mathrm{GeV}$. ID contributions are important for low m_{H}, where there are still many clients for the p_T correction, and the overall effect is a $\sim 4\%$ improvement of the mass resolution. The impact of the m_{Z} constraint has a well pronounced effect on the peak position and also introduces a mass resolution correction, most pronounced at $m_{\mathrm{H}} = 180\,\mathrm{GeV}$, where the improvement reaches 15%.

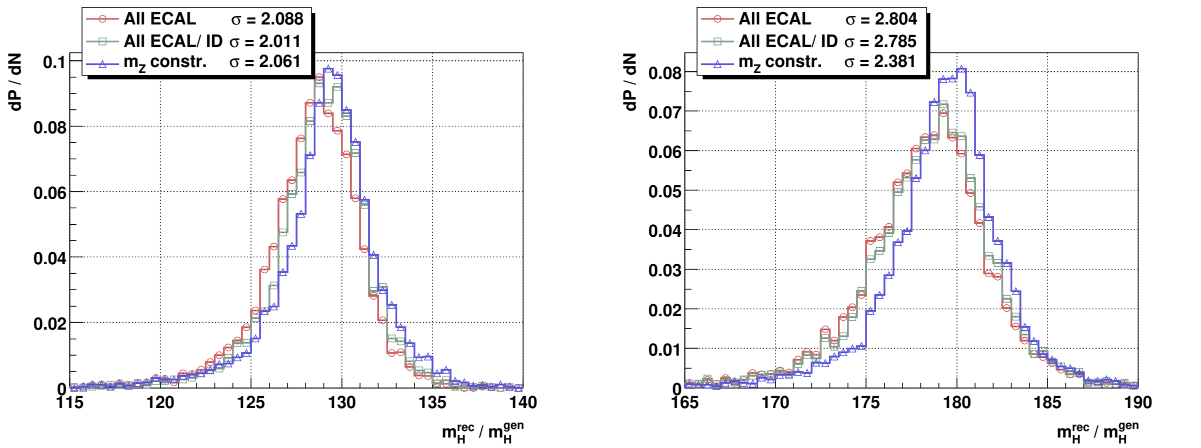

Figure 4.27: Reconstructed m_{H} shapes for $m_{\mathrm{H}} = 130\,\mathrm{GeV}$ (left) and $180\,\mathrm{GeV}$ (right). The plots are labeled by their resolutions. ID corrections were applied for the 'green' sample only.

A more statistical presentation of the results, expressed in statistical terms, is given in Fig:4.28. For comparison, the results obtained without using the m_{Z^0} constraint and ID corrections are also presented. The `no FSR` curve was obtained by discarding all the events for which a FSR photon was detected in the generation banks. The overall effect of the FSR is an increase of the width by about 3%, accompanied by a slender tail on the low-mass-side.

Compared to the *Phyisics Performance TDR* results, the resolutions obtained from **M1/3** event sample are worse by 25% for $m_{\mathrm{H}} = 130, 150\,\mathrm{GeV}$ and by 10% for $m_{\mathrm{H}} = 180\,\mathrm{GeV}$. However, another H → ZZ$^{(\star)}$ → 4e study (at $m_{\mathrm{H}} = 130\,\mathrm{GeV}$), presented in the *Calorimeter*

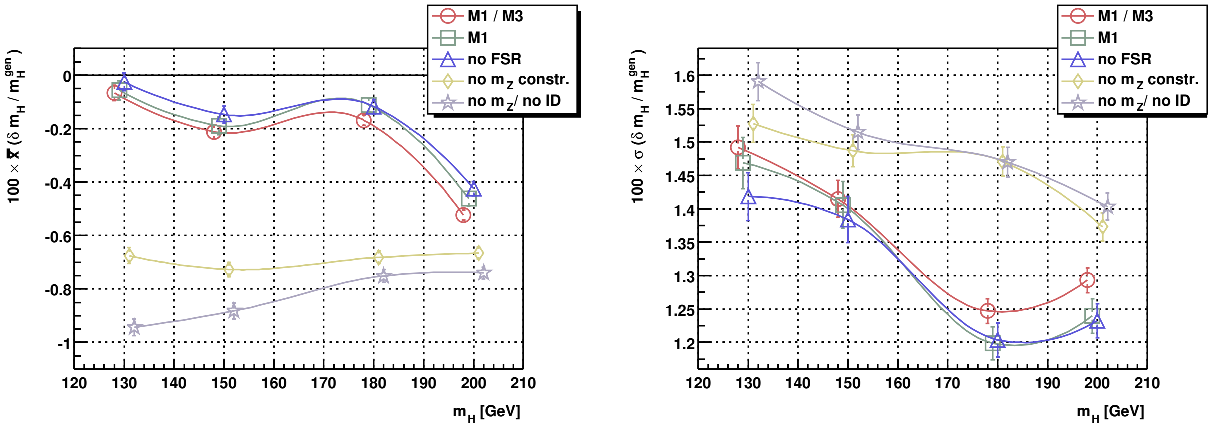

Figure 4.28: Mean value (left) and width (right) of the normalized $m_{\rm H}$ residual distribution as a function of $m_{\rm H}$. The values were obtained from a Gaussian fit in a range from -1.5σ to 2.5σ around the mean. Warning: suppressed zero.

Performance TDR [8], advertises tighter cuts on the mass of the on-shell $\rm Z^0$ ($\pm 6\,\rm GeV$). By applying tighter cuts, the results can be brought in accordance with the ones presented in the TDR. An improvement of about the same size is also achieved by further application of track isolation cuts (no charged tracks with $p_T > 1\,\rm GeV$ in a $d\eta \times d\varphi = 0.1 \times 0.1$ window) at the expense of $\sim 30\%$ loss in efficiency.